Scaling of Magnetic Reconnection in Relativistic Collisionless Pair Plasmas

Yi-Hsin Liu, Fan Guo, William Daughton, Hui Li, and Michael Hesse

Phys. Rev. Lett. **114**, 095002 — Published 3 March 2015

DOI: 10.1103/PhysRevLett.114.095002

Scaling of magnetic reconnection in relativistic collisionless pair plasmas

Yi-Hsin Liu,[1] Fan Guo,[2] William Daughton,[2] Hui Li,[2] and Michael Hesse[1]

[1]*NASA-Goddard Space Flight Center, Greenbelt, MD 20771*
[2]*Los Alamos National Laboratory, Los Alamos, NM 87545*

(Dated: January 27, 2015)

Using fully kinetic simulations, we study the scaling of the inflow speed of collisionless magnetic reconnection in electron-positron plasmas from the non-relativistic to ultra-relativistic limit. In the anti-parallel configuration, the inflow speed increases with the upstream magnetization parameter σ and approaches the speed of light when $\sigma > O(100)$, leading to an enhanced reconnection rate. In all regimes, the divergence of the pressure tensor is the dominant term responsible for breaking the *frozen-in* condition at the x-line. The observed scaling agrees well with a simple model that accounts for the Lorentz contraction of the plasma passing through the diffusion region. The results demonstrate that the aspect ratio of the diffusion region, modified by the compression factor of proper density, remains ~ 0.1 in both the non-relativistic and relativistic limits.

PACS numbers: 52.27.Ny, 52.35.Vd, 98.54.Cm, 98.70.Rz

Introduction– Magnetic reconnection is a process that changes the topology of magnetic fields and often leads to an explosive release of magnetic energy in nature. It is thought to play a key role in many energetic phenomena in space, laboratory and astrophysical plasmas [1]. In recent years, relativistic reconnection has attracted increased attention for its potential of dissipating the magnetic energy and producing high-energy cosmic rays and emissions in magnetically dominated astrophysical systems [2], such as pulsar winds [3–5], gamma-ray bursts [6–8] and jets from active galactic nuclei [9–11]. However, many of the key properties of magnetic reconnection in the relativistic regime remain poorly understood. While early work found the rate of relativistic magnetic reconnection may increase compared to the nonrelativistic case due to the enhanced inflow arising from the Lorentz contraction of plasma passing through the diffusion region [12, 13], it was later pointed out that within a steady-state Sweet-Parker model [14, 15] the thermal pressure within the current sheet will constrain the outflow to mildly relativistic conditions where the Lorentz contraction is negligible [16], and a relativistic inflow is therefore impossible. Recently, the role of temperature anisotropy [17], inflow plasma pressure [18], two-fluid [18], inertia effects [19] and mass ratio [20] have been considered. All existing theories are generalizations of the steady-state Sweet-Parker or Petschek-type [21] models, which do not account for the mechanism that localizes the diffusion region and determines the reconnection rate in collisionless plasmas. Meanwhile, a range of reconnection rates are reported in computational works with different simulation models and normalization definitions [18, 20, 22–25]. However, the scaling of the rate has yet to be determined and the kinetic physics of the diffusion region is poorly understood in the relativistic limit.

In this work, a series of two-dimensional (2D) full particle-in-cell (PIC) simulations have been performed to understand the properties of reconnection in the magnetically dominated regime. It has been argued that electron-positron pairs are relevant in highly energetic astrophysical environment, such as pulsar winds [4, 26] and extragalactic jets [27], hence in this Letter we limit our study to mass ratio $m_i/m_e = 1$. The magnetization parameter can be defined as the ratio of the magnetic energy density to the plasma energy density, $\sigma \equiv B^2/(4\pi w)$ with enthalpy $w = 2n'mc^2 + [\Gamma/(\Gamma-1)]P'$. Here Γ is the ratio of specific heats and $P' \equiv n'(T'_e + T'_p)$ the plasma thermal pressure in the rest frame. The shear Alfvén speed is $V_A = c[\sigma/(1+\sigma)]^{1/2}$ [18, 28–30]. In this Letter, the primed quantities are measured in the fluid rest (proper) frame, while the unprimed quantities are measured in the simulation frame unless otherwise specified. As pointed out in Ref. [16], if a simple pressure balance $P' \sim B^2/8\pi$ is satisfied across a steady-state Sweet-Parker layer, this will constrain the effective $\sigma \sim O(1)$, and thus restrict the inflow speed $V_{in} \ll c$. However, we demonstrate the development of relativistic inflows when the upstream $\sigma > O(100)$ (for the first time) in fully kinetic simulations. A simple model based on the underlying idea of Blackman and Field [12] is presented to explain the scaling of the inflow speed and normalized reconnection rate. It is well known that the normalized collisionless reconnection rate, $R = V_{in}/V_{Ax} \sim 0.1$, in the non-relativistic limit can be estimated by the aspect ratio of the diffusion region, but the precise physics that determines this value remains mysterious [31]. Here V_{Ax} is the Alfvén wave velocity in the outflow direction. Interestingly, the simulation results in this study suggest that this aspect ratio (modified by the compression factor of proper density at the inflow and outflow) of ~ 0.1 persists in the relativistic regime. In addition, we analyze the relativistic generalization of Ohm's law [32], and identify the importance of the pressure tensor and the time-derivative of the inertial term in breaking the *frozen-in* condition.

Simulation setup– The majority of simulations in this letter start from a relativistic Harris sheet [22, 33–35].

The initial magnetic field $\mathbf{B} = B_0\tanh(z/\lambda)\hat{\mathbf{x}} + B_g\hat{\mathbf{y}}$ corresponds to a layer of half-thickness λ with a shear angle $\phi = 2\tan^{-1}(B_0/B_g)$. Each species has a distribution $f_h \propto \mathrm{sech}^2(z/\lambda)\exp[-\gamma_d(\gamma_L mc^2 + mV_d u_y)/T']$ in the simulation frame, which is a component with a peak density n_0' and temperature T' boosted by a drift velocity $\pm V_d$ in the y-direction for positrons and electrons, respectively. Here $\mathbf{u} = \gamma_L\mathbf{v}$ is the spacelike components of 4-velocity, $\gamma_L = 1/[1-(v/c)^2]^{1/2}$ is the Lorentz factor of a particle, and $\gamma_d \equiv 1/[1-(V_d/c)^2]^{1/2}$. The drift velocity is determined by Ampére's law $cB_0/(4\pi\lambda) = 2e\gamma_d n_0' V_d$. The temperature is determined by the pressure balance $B_0^2/(8\pi) = 2n_0'T'$. The resulting density in the simulation frame is $n_0 = \gamma_d n_0'$. In addition, a non-drifting background component $f_b \propto \exp(-\gamma_L mc^2/T_b)$ with a uniform density n_b is included. The simulations are performed using VPIC [36], which solves the fully relativistic dynamics of particles and electromagnetic fields. Densities are normalized by the initial background density n_b, time is normalized by the plasma frequency $\omega_{pe} \equiv (4\pi n_b e^2/m_e)^{1/2}$, velocities are normalized by the light speed c, and spatial scales are normalized by the inertia length $d_e \equiv c/\omega_{pe}$. Although commonly used, the relativistic Harris sheet may not be generic. To test the sensitivity of our results to the initial sheet equilibrium, a force-free configuration [25, 37] was also included, with magnetic profile $\mathbf{B} = B_0\tanh(z/\lambda)\hat{\mathbf{x}} + [B_g^2 + B_0^2\mathrm{sech}(z/\lambda)]^{1/2}\hat{\mathbf{y}}$, and uniform density and temperature. Particles in the central sheet have a net drift $\mathbf{V}_p = -\mathbf{V}_e$ to satisfy Ampére's law. All simulations use $100-200$ particles per cell for each species (supplement D shows a convergence study). The boundary conditions are periodic in the x-direction, while in the z-direction the boundary conditions are conducting for fields and reflecting for particles. A localized perturbation with amplitude $B_z = 0.03B_0$ is used to induce a dominant x-line near the center of simulation domain. The simulation parameters for the various runs considered in this Letter are summarized in Table 1. Our primary focus in the following section is the case Harris-4 which illustrates the dynamics in the transition to the limit with relativistic inflows (*i.e.,* $V_{in} \approx c$). The domain size is $L_x \times L_z = 384d_e \times 384d_e$ with 3072×6144 cells. The half-thickness of the initial sheet is $\lambda = d_e$, $n_b = n_0'$, $T_b/mc^2 = 0.5$, $B_g = 0$ and $\omega_{pe}/\Omega_{ce} = 0.05$ where $\Omega_{ce} \equiv eB_0/(m_e c)$ is the cyclotron frequency. The upstream magnetization parameter based on the reconnecting component is $\sigma_x \equiv B_0^2/(4\pi w) = (\Omega_{ce}/\omega_{pe})^2/\{2[1+(\Gamma/(\Gamma-1))(T_b/mc^2)]\}$, which is 88.9 with $\Gamma = 5/3$. For cases with $T_b/mc^2 > 1$ in Table 1, we use $\Gamma = 4/3$ [38, 39].

Simulation results– Fig. 1(a) shows the structure of current sheet in the nonlinear stage, where the current density concentrates within a layer with a half-thickness $\sim d_e$. This thickness appears to be independent of the initial sheet thickness, and scales with the inertial length based on the asymptotic background density (n_b). As

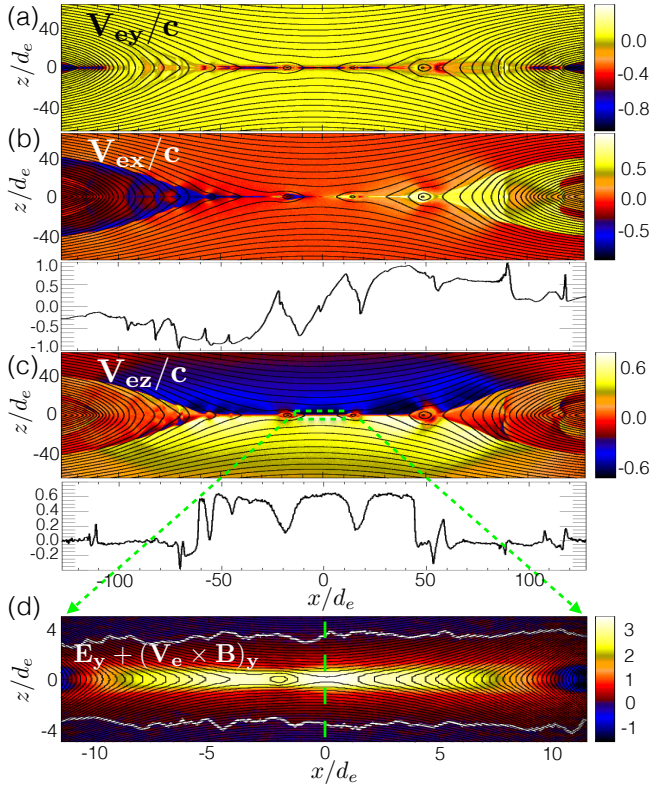

FIG. 1: Results from case Harris-4 ($\sigma = \sigma_z = 88.9$) during the fully nonlinear phase at $566.4/\omega_{pe}$ showing (a) the electron out-of-plane speed V_{ey}, (b) outflow speed V_{ex} with cut at $z = 0$, (c) inflow speed V_{ez} with cut at $z = -3.5d_e$, (d) a closeup showing the non-ideal electric field $E_y + (\mathbf{V}_e \times \mathbf{B})_y$ inside the green-dashed box depicted in (c). The non-ideal electric field is positive in between the horizontal white curves. Black contours are flux surfaces in (a)-(d).

shown in Fig. 1(b), the outflow velocity approaches $\sim c$, while in Fig. 1(c) the peak inflow speed is $\sim 0.65c$. Note that these relativistic inflows also penetrate deeply across the magnetic separatrix into the d_e-scale sheet in the downstream region ($|x| \sim 50d_e$). In addition, the simulation shows a rapid growth of secondary tearing modes, not only around the major x-line, but also along the concentrated current sheet that extends into the outflow exhausts. Interestingly, the secondary tearing mode appears considerably shorter spatially in comparison with those in the non-relativistic regime. As shown in the blow-up (Fig. 1(d)), a magnetic island at ($x \sim -2d_e, z = 0$) is immersed inside the region where the *frozen-in* condition is broken, and it has a size $\sim 3d_e \times 2d_e$, implying that the secondary tearing mode grows for wave vectors $k_x\bar{\delta} > 1$. Here $\bar{\delta}$ is the half-thickness of the intense nonlinear current layer. In contrast, the initial tearing mode based on the relativistic Harris equilibrium is still constrained by $k_x\lambda < 1$ (*i.e.,* from relativistic energy principle) [40], as in the non-relativistic limit. A temperature anisotropy [41, 42]

or the velocity shear associated with the outflow jet [43–45] may change the stability criterion, however, to resolve this issue in the relativistic regime is beyond the scope of this Letter. Fig. 1(d) shows that the non-ideal electric field is also concentrated in a region $|z| < d_e$. However, the *frozen-in* condition starts to fail inside a wider layer in between the horizontal white curves, which may be due to a larger effective inertial scale based on a smaller density at $|z| \gtrsim d_e$ (see the density cut in Fig. 2(a)). Fig. 2(a) shows that the inflow velocity V_{ez} reaches its maximum $\sim 0.65c$ at the location where *frozen-in* starts to fail (*i.e.,* marked by the green circle on the $E_y + (\mathbf{V}_e \times \mathbf{B})_y$ curve). The profile of V_{ez} is rather flat in between this location and $z = d_e$. Motivated by this observation, we use the local magnetic field $B_{x,u}$ at this location ($z \sim 3.5d_e$) to normalize the reconnection electric field E_y, and the normalized electric field traces the evolution of the peak inflow velocity well (Fig. 2(b)), as expected. Since in this relativistic regime $V_{Ax} \approx c$, these two quantities are equivalent measurements of the normalized reconnection rate as discussed in the following section. The original peak density at the center of the sheet is $n_0 + n_b = \gamma_d + 1 \approx 11$. This peak density drops significantly from 11 to ~ 2 and the density along the symmetry line ($z = 0$) remains $\sim 2 - 4$, except inside secondary islands. The density ratio between the region immediately upstream to the x-line is $\sim 2.5/0.3 = 8.3$. These numbers will be used to estimate the compression factor in the following section. Per Ampeŕe's law, the density changes inside this d_e-scale layer require a reduction of the local magnetic field since the motion of the current carrier is limited by the speed of light [46].

To examine the mechanism of flux breaking, we employ the relativistic generalization of Ohm's law $\mathbf{E} + \mathbf{V}_e \times \mathbf{B} + (1/en_e)\nabla \cdot \overleftrightarrow{P}_e + (m_e/e)(\partial_t \mathbf{U}_e + \mathbf{V}_e \cdot \nabla \mathbf{U}_e) = 0$. Here $\mathbf{U} \equiv (1/n) \int d^3u \mathbf{u} f$, and the fluid velocity is $\mathbf{V} \equiv (1/n) \int d^3u \mathbf{v} f$. The pressure tensor, $\overleftrightarrow{P} \equiv \int d^3u \mathbf{v}\mathbf{u} f - n\mathbf{V}\mathbf{U}$, defined in this manner reduces to the standard definition in the non-relativistic regime [32]. Each term along the vertical cut in Fig. 1(d) is plotted in Fig. 2(c). There are strong oscillations in both $\nabla \cdot \overleftrightarrow{P}_e$ and $\mathbf{V}_e \cdot \nabla \mathbf{U}_e$, which largely cancel each other. In comparison, the magnitude of the non-ideal electric field $E_y + (\mathbf{V}_e \times \mathbf{B})_y$ is much smaller. In Fig. 2(d), we examine the region around the neutral point, which demonstrates that $\mathbf{V}_e \cdot \nabla \mathbf{U}_e$ vanishes at $z = 0$ since the neutral point coincides with the stagnation point in this symmetric configuration. The thermal pressure term, $\nabla \cdot \overleftrightarrow{P}_e$, balances the non-ideal electric field at the x-line while the time-derivative of the inertia $\partial_t \mathbf{U}_e$ remains small at this time [32], consistent with the study in the non-relativistic limit [47–50]. However, the intense current layer is strongly unstable to secondary tearing modes, similar to the non-relativistic limit [51]. The time-derivative of inertia $\partial_t \mathbf{U}_e$ becomes finite positive when the d_e-scale current layer extends in length, and $\partial_t \mathbf{U}_e$ becomes finite negative (*i.e.,* contributing to reconnection) when a secondary tearing starts to emerge in a sufficiently long layer (supplement B).

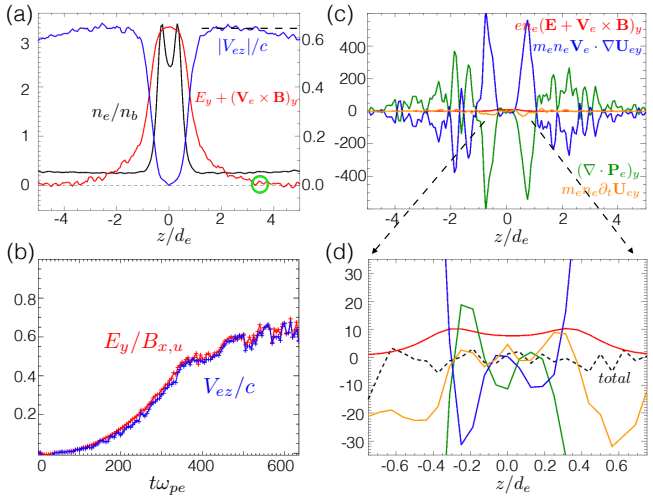

FIG. 2: In (a), n_e, $E_y + (\mathbf{V}_e \times \mathbf{B})_y$ and $|V_{ez}|$ along the vertical cut shown in Fig. 1(d). $|V_{ez}|$ is scaled by the right axis. The green circle marks the location where the *frozen-in* condition starts to fail; In (b), the evolution of the normalized reconnection electric field $E_y/B_{x,u}$ and the peak V_{ez} near the major x-line at $\min(A_y)$ along $z = 0$. Here A_y is the y-component of vector potential; In (c), quantities of Ohm's law along the vertical cut shown in Fig. 1(d); In (d), the blow-up of (c) near the magnetic neutral point.

Simple model– While previous theories [12, 13, 16, 19] generalize the Sweet-Parker [14, 15] or Petschek's [21] models into the relativistic regime, here we simply analyze the conservation of mass including the influence of the Lorentz contraction over a control-volume of size $L \times \delta$,

$$V_{in}\gamma_{in}n'_{in}L = V_{out}\gamma_{out}n'_{out}\delta. \tag{1}$$

Here the subscript "*in*" and "*out*" indicate the inflowing and outflowing plasmas, respectively. Given a magnetic shear angle, the outflow is limited by the upstream Alfveń wave velocity projected into the x-direction [31],

$$V_{out} = V_{Ax} = c\sqrt{\frac{\sigma_x}{1+\sigma}}. \tag{2}$$

Here the upstream magnetization parameter is $\sigma = \sigma_x + \sigma_g$ with $\sigma_g \equiv B_g^2/(8\pi w)$ accounting for the contribution from the guide field. The effective Lorentz factor based on the bulk flows is $\gamma_{out} = 1/[1 - (V_{out}/c)^2]^{1/2} = [(1+\sigma)/(1+\sigma_g)]^{1/2}$ and $\gamma_{in} = \{(1+\sigma)/[1+\sigma - \sigma_x(V_{in}/V_{Ax})^2]\}^{1/2}$.

Working through the algebra, the peak inflow velocity can be determined with only one free parameter, $r_{n'}\delta/L$,

$$\frac{V_{in}}{c} = \left(r_{n'}\frac{\delta}{L}\right)\sqrt{\frac{\sigma_x}{1+\sigma_g+(r_{n'}\delta/L)^2\sigma_x}}, \tag{3}$$

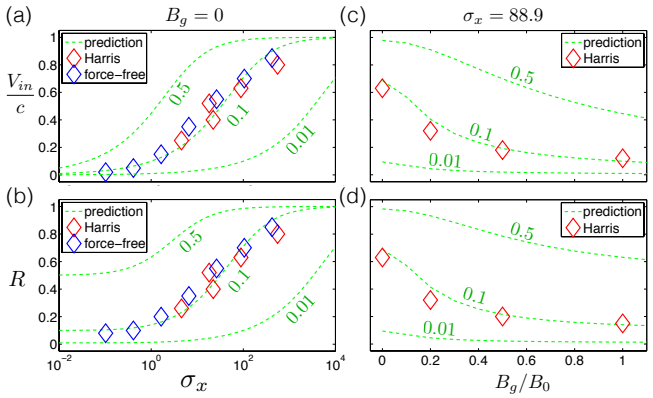

FIG. 3: Scaling of the inflow velocity V_{in}/c and the normalized reconnection rate R as a function of σ_x for cases with $B_g = 0$ in the left; as a function of B_g/B_0 for cases with $\sigma_x = 88.9$ in the right. Diamonds are measurements of runs in Table 1, green-dashed curves are predictions based on different value of $r_{n'}\delta/L$ as marked on the plots.

where $r_{n'} \equiv n'_{out}/n'_{in}$ is the proper density ratio of the outflow to inflow. The compression factor is

$$\frac{n_{out}}{n_{in}} = r_{n'}\sqrt{\frac{1+\sigma}{1+\sigma_g+(r_{n'}\delta/L)^2\sigma_x}}, \tag{4}$$

and the normalized reconnection rate is

$$R \equiv \frac{V_{in}}{V_{Ax}} = \left(r_{n'}\frac{\delta}{L}\right)\sqrt{\frac{1+\sigma}{1+\sigma_g+(r_{n'}\delta/L)^2\sigma_x}}. \tag{5}$$

Note that R differs from V_{in}/c by a factor c/V_{Ax}. From the *frozen-in* condition, the normalized rate can also be written as $R = (c/V_{Ax})E_y/B_{x,u}$. In the limit of $V_{Ax} \to c$, then $R \sim V_{in}/c \sim E_y/B_{x,u}$ as shown in Fig. 2(b).

With the assumption of $r_{n'}\delta/L = 0.1$, as in the non-relativistic limit, Eqs. (3) and (5) immediately give $R \sim V_{in}/c = 0.69$, consistent with the observed values for the case discussed. By comparing the measured compression factor ~ 8.3 in Fig. 2(a) and $n_{out}/n_{in} = 6.9r_{n'}$ from Eq (4), this implies that $r_{n'} \sim O(1)$ and therefore the aspect ratio $\delta/L \sim O(0.1)$. The aspect ratio of the intense $E_y+(\mathbf{V}_e\times\mathbf{B})_y$ layer shown in Fig. 2(d) seems to be consistent with this idea, however, a definite measurement is difficult because of time-dependency (more in supplement C). To further test these predictions, a series of runs were performed over a wide range of parameters (listed in Table 1). The measurement of V_{in}/c and R are shown in Fig. 3 as diamonds, which agree closely with the predicted scaling based on $r_{n'}\delta/L = 0.1$. This suggests that the modified aspect ratio of the diffusion region persists during the transition from the non-relativistic to strongly relativistic regime. With a larger σ_x, both the outflow and inflow speeds become closer to the speed of light. For anti-parallel initial conditions (*i.e.,* $\sigma_g = 0$), both V_{in}/c and R approach unity only when $\sigma_x > O(100)$, as shown in Fig. 3 (a)-(b), a condition obtained by demanding $(r_{n'}\delta/L)^2\sigma_x = 0.01\sigma_x \gg 1$ in the denominator of Eq. (3) and (5). On the other hand, with a guide field $B_g/B_0 \gtrsim O(1)$, the outflow speed (Eq.(2)) becomes non-relativistic, the Lorentz contraction becomes negligible and the reconnection rate therefore goes back to ~ 0.1 as shown in Fig. 3(d). To test the dependence on the choice of initial conditions, we have also performed an additional series of simulations using a force-free current sheet for initial condition [25]. The final states are similar to those of initial Harris sheets and the measurement shown as blue diamonds in Fig. 3(a)-(b) follow the same trend, which demonstrates that the scaling in the nonlinear stage is determined solely by the upstream condition. Our model appears to explain the scaling of the normalized rate observed in two-fluid simulations of Zenitani et. al. [18] as well. Unfortunately, due to the complexity of evolution in the nonlinear phase, we are not able to predict the reconnection rate normalized by the far upstream reconnecting component, which approaches a maximum of ~ 0.3 for cases with $\sigma_x \sim O(500)$ in the present study.

Discussion– During the initial evolution of Harris-type current sheets, the pressure balance argument proposed in Ref. [16] restricts the inflow to $V_{in} \ll c$. However, at later times there are a variety of features which may break this argument. Firstly, the repeated formation of secondary plasmoids makes the diffusion region highly time-dependent. Secondly, the current density inside each of these plasmoids is much stronger than the current density within the diffusion regions between the plasmoids. This redistribution of current alters the structure of the reconnection layer and leads to strong variations in the reconnecting component of the upstream magnetic field. As a result, the plasma pressure and density around the x-line drop significantly from the initial sheet value (see Supplement A for pressure balance). This fact may reduce the impediment that slows the Alfvénic outflows. For cases with a higher upstream σ, the initial sheet component is denser and hotter. The system takes a longer time to deplete this sheet component and develop relativistic inflows, as suggested by the comparison of the time-scale between Harris-3 and 5 cases in Table 1.

In summary, a simple theory based on the Lorentz contraction [12] and the assumption of a universal aspect ratio (~ 0.1) of the diffusion region provides an explanation for the observed relativistic inflows and the enhanced normalized reconnection rate. While the present letter was limited to 2D simulations, recent 3D simulations demonstrate similar relativistic inflows in spite of the development of kink instabilities [52]. These results may be important for understanding particle acceleration [25, 53], the dissipation of strong magnetic field in high-energy astrophysical systems, such as the "σ-problem" in the Crab Nebula [33], and the destruction of strong magnetic field near magnetars [6] and black holes [9].

Y.-H. Liu thanks for helpful discussions with S. Zeni-

TABLE I: Paramters of Runs

Harris	1	2	3	4	5	6	7	8
B_g/B_0	0	0	0	0	0	0.2	0.5	1
n_b/n_0'	1	0.25	1	1	1	1	1	1
T_b/mc^2	2.5	2.5	0.5	0.5	0.5	0.5	0.5	0.5
ω_{pe}/Ω_{ce}	0.1	0.05	0.1	0.05	0.02	0.05	0.05	0.05
σ_x	4.5	18.2	22.2	88.9	555.6	88.9	88.9	88.9
time$\times\omega_{pe}$ [a]	200	100	250	500	1000	400	350	300
Force-Free	1	2	3	4	5	6	7	
B_g/B_0	0	0	0	0	0	0	0	
T_b/mc^2	0.35	0.36	0.36	0.36	0.36	0.36	0.36	
ω_{pe}/Ω_{ce}	1.6	0.8	0.4	0.2	0.1	0.05	0.025	
σ_x	0.1	0.4	1.6	6.6	26.3	105.3	421	

[a] the time when V_{in} reaches a steady high value

tani, N. Bessho and J. Tenbarge. We are grateful for support from NASA through the NPP program and the Heliophysics Theory program. Simulations were performed at the National Center for Computational Sciences at ORNL and with LANL institutional computing.

[1] H. Ji and W. Daughton, Phys. Plasmas **18** (2011).
[2] M. Hoshino and Y. Lyubarsky, Space Sci. Rev. **173**, 521 (2012).
[3] F. V. Coroniti, Astrophys. J. **349**, 538 (1990).
[4] J. Arons, Space Sci. Rev. **173**, 341 (2012).
[5] Y. Lyubarsky and J. G. Kirk, Astrophys. J. **547**, 437 (2001).
[6] C. Thompson, Mon. Not. R. Astron. Soc. **270**, 480 (1994).
[7] B. Zhang and H. Yan, Astrophys. J. **726**, 90 (2011).
[8] J. C. McKinney and D. A. Uzdensky, Mon. Not. R. Astron. Soc. **419**, 573 (2012).
[9] K. Beckwith, J. F. Hawley, and J. H. Krolik, Astrophys. J. **678**, 1180 (2008).
[10] D. Giannios, Mon. Not. R. Astron. Soc. **408**, L46 (2010).
[11] C. H. Jaroschek, H. Lesch, and R. A. Treumann, Astrophys. J. **605**, L9 (2004).
[12] E. G. Blackman and G. B. Field, Phys. Rev. Lett. **72**, 494 (1994).
[13] M. Lyutikov and D. Uzdensky, Astrophys. J. **589**, 893 (2003).
[14] P. A. Sweet, in *IAU Symp. in Electromagnetic Phenomena in Cosmical Physics, ed. B. Lehnet (New York: Cambridge Univ. Press)* (1958), p. 123.
[15] E. N. Parker, J. Geophys. Res. **62**, 509 (1957).
[16] Y. E. Lyubarsky, MNRAS **358**, 113 (2005).
[17] J. M. Tenbarge, R. D. Hazeltine, and S. M. Mahajan, Mon. Not. R. Astron. Soc. **403**, 335 (2010).
[18] S. Zenitani, M. Hesse, and A. Kimas, Astrophys. J. **696**, 1385 (2009).
[19] L. Comisso and F. A. Asenjo, Phys. Rev. Lett. **113**, 045001 (2014).
[20] M. Melzani, R. Walder, D. Folini, C. Winisdoerfer, and J. M. Favre, A & A **570**, A111 (2014).
[21] H. E. Petschek, in *Proc. AAS-NASA Symp. Phys. Solar Flares* (1964), vol. 50 of *NASA-SP*, pp. 425–439.
[22] N. Bessho and A. Bhattacharjee, Astrophys. J. **750**, 129 (2012).
[23] B. Cerutti, G. R. Werner, D. A. Uzdensky, and M. C. Begelman, Astrophys. J. Lett. **754**, L33 (2012).
[24] L. Sironi and A. Spitkovsky, Astrophys. J. **783**, L21 (2014).
[25] F. Guo, H. Li, W. Daughton, and Yi-Hsin Liu, Phys. Rev. Lett. **113**, 155005 (2014).
[26] P. A. Sturrock, Astrophys. J. **164**, 529 (1971).
[27] J. Wardle, D. Homan, R. Ojha, and D. H. Roberts, Nature **395**, 457 (1998).
[28] J. Sakai and T. Kawata, J. Phy. Soc. Japan **49**, 747 (1980).
[29] A. M. Anile, *Relativistic Fluids and Magneto-Fluids* (Cambridge University Press, New York, 1989), chap. 2, p. 34.
[30] A. Lichnerowicz, *Relativistic Hydrodynamics and Magnetohydrodynamics* (W. A. Benjamin Inc., New York, 1967), chap. 4, p. 112.
[31] Yi-Hsin Liu, W. Daughton, H. Karimabadi, H. Li, and S. P. Gary, Phys. Plasmas **21**, 022113 (2014).
[32] M. Hesse and S. Zenitani, Phys. Plasmas **14**, 112102 (2007).
[33] J. G. Kirk and O. Skjeraasen, Astrophys. J. **591**, 366 (2003).
[34] S. Zenitani and H. Hoshino, Astrophys. J. **670**, 702 (2007).
[35] W. Liu, H. Li, L. Yin, B. J. Albright, K. J. Bowers, and E. P. Liang, Phys. Plasmas **18** (2011).
[36] K. Bowers, B. Albright, L. Yin, W. Daughton, V. Roytershteyn, B. Bergen, and T. Kwan, Journal of Physics: Conference Series **180**, 012055 (2009).
[37] Yi-Hsin Liu, W. Daughton, H. Karimabadi, H. Li, and V. Roytershteyn, Phys. Rev. Lett. **110**, 265004 (2013).
[38] S. Weinberg, *Gravitation and Cosmology: Principle and Applications of the central theory of relativity* (John Wiley and Sons, Inc, New York, 1972), chap. 2, p. 51.
[39] J. L. Synge, *The Relativitic Gas* (North-Holland Publication Company, Amsterdam, 1957), chap. 6, p. 60.
[40] A. Otto and K. Schindler, Plasma Phys. Control. Fusion **26**, 1525 (1984).
[41] H. Karimabadi, W. Daughton, and K. B. Quest, Geophys. Res. Lett. **32**, L18801 (2004).
[42] L. Matteini, S. Landi, M. Velli, and W. H. Matthaeus, Astrophys. J. **763**, 142 (2013).
[43] M. Hoshino and K. Higashimori, submitted to J. Geophys. Res. (2015).
[44] M. Shigeta, T. Sato, and B. Dasgupta, J. Phys. Soc. Japan **54**, 3342 (1985).
[45] S. Wang, L. C. Lee, and C. Q. Wei, Phys. Fluids **31**, 1544 (1988).
[46] S. Zenitani and M. Hesse, Astrophys. J. **684**, 1477 (2008).
[47] M. Hesse, K. Schindler, J. Birn, and M. Kuznetsova, Phys. Plasmas **6**, 1781 (1999).
[48] M. Hesse, M. Kuznetsova, and J. Birn, Phys. Plasmas **11**, 5387 (2004).
[49] P. Ricci, J. U. Brackbill, W. Daughton, and G. Lapenta, Phys. Plasmas **11**, 4102 (2004).
[50] P. L. Pritchett and F. V. Coroniti, J. Geophys. Res. **109**, A01220 (2004).
[51] W. Daughton and H. Karimabadi, Phys. Plasmas **14**, 072303 (2007).
[52] F. Guo, Yi-Hsin Liu, W. Daughton, and H. Li, in preparation (2015).

[53] S. Zenitani and H. Hoshino, Astrophys. J. **562**, L63 (2001).